JACS
JOURNAL OF THE AMERICAN CHEMICAL SOCIETY

Article

pubs.acs.org/JACS

Thermodynamics of Phase Selection in MnO_2 Framework Structures through Alkali Intercalation and Hydration

Daniil A. Kitchaev,*[,†] Stephen T. Dacek,[†,§] Wenhao Sun,[†,‡,§] and Gerbrand Ceder*[,†,‡,∥]

[†]Department of Materials Science and Engineering, MIT, Cambridge, Massachusetts 02139, United States
[‡]Materials Science Division, LBNL, Berkeley, California 94720, United States
[∥]Department of Materials Science and Engineering, UC Berkeley, Berkeley, California 94720, United States

Supporting Information

ABSTRACT: While control over crystal structure is one of the primary objectives in crystal growth, the present lack of predictive understanding of the mechanisms driving structure selection precludes the predictive synthesis of polymorphic materials. We address the formation of off-stoichiometric intermediates as one such handle driving polymorph selection in the diverse class of MnO_2-framework structures. Specifically, we build on the recent benchmark of the SCAN functional for the *ab initio* modeling of MnO_2 to examine the effect of alkali-insertion, protonation, and hydration to derive the thermodynamic conditions favoring the formation of the most common MnO_2 phases—β, γ, R, α, δ, and λ—from aqueous solution. We explain the phase selection trends through the geometric and chemical compatibility of the alkali cations and the available phases, the interaction of water with the system, and the critical role of protons. Our results offer both a quantitative synthesis roadmap for this important class of functional oxides, and a description of the various structural phase transformations that may occur in this system.

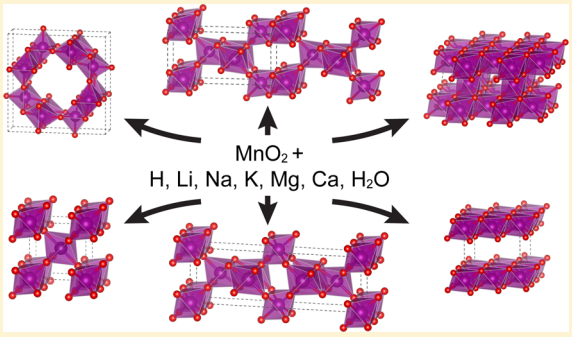

INTRODUCTION

As the *ab initio* design of materials with a set of prescribed properties is making significant advances,[1] the synthesis of such novel compounds is often a practical and time-consuming obstacle to their realization. This is particularly true for phases that are metastable for which high-temperature solid-state synthesis routes cannot be used. Understanding better how specific synthesis conditions lead to a particular phase is a first step to the ultimate goal of inverting this relation and designing synthesis routes that target a specific polymorph. In this paper we use MnO_2 as a prototype system with a high degree of polymorphism to understand the chemical handles that lead to the formation of a specific solid phase. The diverse modifications of MnO_2, formed through a variety of off-stoichiometric intermediates, have been widely studied as Li-ion battery cathodes,[2,3] photocatalysts,[4,5] molecular sieves,[6] supercapacitors,[7] and pigments,[8] where each application requires a specific MnO_2 structural polymorph[9] or structural motif in the case of nanocrystalline manganese oxides.[4] Despite an abundance of literature reporting synthesis recipes for each MnO_2 polymorph and documenting the transformations between them, the understanding of the underlying driving forces is sparse. This gap in the present knowledge of the manganese oxide system makes it difficult to separate kinetic effects from thermodynamics in any mechanistic analysis of MnO_2 formation, or to make quantitative predictions regarding phase transformations, which limit both the scientific understanding of manganese dioxide chemistry and the design of functional MnO_2-based materials.

The most common structures accessible by aqueous synthesis in the manganese dioxide system are the rutile-type β phase, hollandite-type α, ramsdellite-type R, birnessite-type δ, spinel-type λ, and γ, which is an intergrowth of β and R with various fractions of β/R domains and twinning.[10,12] These six structures are shown in Figure 1, which illustrates their overall framework, as well as their approximate low temperature magnetic configuration and predicted interstitial sites. Importantly, we consider a single prototypical γ structure that is a 50% mixture of β and R domains, as a model of the general class of such intergrowth phases.[12,13] All of these structures consist of corner- and edge-sharing MnO_6 octahedra which pack to form a hexagonal-close-packed (HCP) oxygen sublattice in the case of β, α, R, γ, and O1-stacked δ,[11] or a face-centered-cubic (FCC) oxygen sublattice in the case of λ and O3-stacked δ.[11] In terms of their magnetic structure, all MnO_2 polymorphs are well-represented as relatively simple antiferromagnets,[10,14−16] although the true magnetic structure of certain polymorphs is more complex.[17,18] The packings of MnO_6 octahedra create a variety of voids that form sublattices of structurally equivalent interstitial sites, which allow the intercalation of cations and water into the MnO_2 frameworks.

Received: October 31, 2016
Published: January 31, 2017

DOI: 10.1021/jacs.6b11301
J. Am. Chem. Soc. 2017, 139, 2672−2681

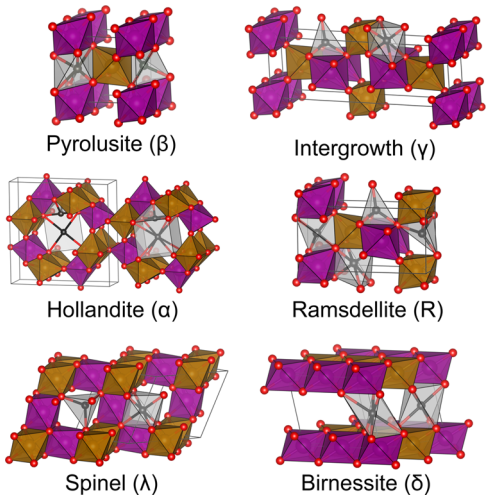

Figure 1. Common polymorphs of MnO_2 and predicted sites for alkali intercalation. The purple and yellow spheres and surrounding octahedra denote spin-up and spin-down Mn atoms and MnO_6 octahedra,[10] while the black spheres and surrounding gray polyhedra denote potential intercalation sites for alkali and alkali-earth ions in the structure. Each site shown defines a distinct sublattice—while a single site of each type is shown, all equivalent sites are included in the structural enumeration. Note that for the birnessite (δ) phase we consider the monoclinic O1-stacked ($P\bar{3}m1$) and O3-stacked ($R\bar{3}m$) (shown) configurations as competing configurations of the same phase.[11] Furthermore, while the γ phase generally refers to a range of intergrowth structures with a varying fraction of β-like and R-like domains, we choose a representative structure with 50% β-type tunnels for the purposes of all calculations.

Given the diverse applications of MnO_2 polymorphs, there are a number of established synthesis methods that yield phase-pure forms of each structure.[9,19−24] The β, α, R, λ, and δ forms can be made hydrothermally from an aqueous solution containing Mn^{2+} or MnO_4^-, as well as some alkali or alkali-earth cations. The γ phase, also known as "electrolytic manganese oxide" (EMD), is a common product in high-rate electrochemical deposition, typically from an aqueous solution of $MnSO_4$ and H_2SO_4, although this phase can also be made hydrothermally as "chemical manganese oxide" (CMD).[12,25,26] While the synthesized products often contain significant amounts of intercalated alkali or alkali-earth cations, protons, and/or water, mild postprocessing of the as-synthesized product can yield stoichiometrically pure forms of the various MnO_2 polymorphs without any intercalated ions.[19,21,22,27] In other cases, however, the extraction of intercalants from the MnO_2 framework induces phase transformations, suggesting that the cations play a key role in kinetically or thermodynamically stabilizing the polymorphs during initial phase selection,[22,28] consistent with the results of several *in situ* studies.[29,30] These results motivate our work on establishing a thermodynamic baseline for the stability of off-stoichiometric intercalated MnO_2-type phases, both for distinguishing thermodynamic and kinetics effects, and for guiding the targeted synthesis of MnO_2 structures through off-stoichiometric intermediates.

Previous work on characterizing the thermodynamics of the alkali-containing manganese oxides has yielded partial data on the nature of the driving forces governing phase selection. Calorimetry on several naturally occurring MnO_2-framework type minerals[31,32] gave an early indication of the critical importance of alkali cations in the thermodynamic stabilization of a number of MnO_2 frameworks. Subsequent computational work has reproduced several of these pathways. For example, based on a density functional theory (DFT) analysis, Reed et al. report the destabilization of δ-MnO_2 with respect to λ under Li^+ intercalation,[33] Balachandran et al. identify the importance of structural water in stabilizing R over β,[34] Cockayne et al. and Wei et al. study the stabilization of α and δ with respect to β by dilute K^+ intercalation and hydration,[35,36] Tompsett et al. and Wang et al. model the destabilization of the α and β frameworks respectively under Li^+ intercalation,[37,38] while Ling et al. calculate the conversion α to λ on Mg^{2+} insertion.[39] In a recent work, Li et al. computationally hypothesize a number of possible mechanisms for the transformation from δ to the β, R, α, and related tunnel structures. In all cases, computational work has been limited to a subset of MnO_2 phases and alkali-ions, typically focusing on fixed-composition or single-phase (topotactic) reactions. While these data give insight into a subset of possible reactions in the manganese dioxide system, an analysis of MnO_2 synthesis pathways requires a grand-potential approach that considers all possible phases and compositions. Previously, such an analysis was not possible as existing *ab initio* methods failed to give accurate results for the relative energetics of MnO_2 polymorphs.[10] The recent resolution of these methodological difficulties through the SCAN exchange-correlation functional[10,40] enables us to establish a consistent model of alkali−MnO_2 thermodynamics across all phases and compositions.

In this work, we construct a comprehensive thermodynamic baseline for the common polymorphs of MnO_2 in an aqueous environment, accounting for the effect of water, as well as H^+, Li^+, Na^+, K^+, Mg^{2+}, and Ca^{2+} ions. Importantly, we consider all MnO_2-derived phases across all dry and hydrated ternary compositions to offer a reliable energetic ranking of MnO_2 polymorphs across a variety of stoichiometries. In addition to establishing thermodynamic boundary conditions for the aqueous synthesis of MnO_2 structures, our data yield a full set of potential "energetically downhill" phase transformations in the system, which are critical data for the prediction of transformation pathways between the polymorphs under nonequilibrium conditions, the evaluation of classical and nonclassical nucleation pathways,[41] and the interpretation of *in situ* data. Finally, our analysis reveals the evolution of the driving force for phase transformation upon the extraction or insertion of cations, which is of interest for estimating the feasibility of topotactic reactions in this space.

More generally, the MnO_2 system, whose diverse polymorphism arises from an array of intercalation redox reactions that allow each phase to accommodate significant off-stoichiometry, is an ideal model system to analyze the coupling between redox activity in transition metal ceramics and the diversity of their structures. As we discuss here, the types of intercalation sites created by each transition-metal framework determine which structures can be synthesized in the presence of alkali and alkali-earth ions of varying size and valency, as well as water. As such, we establish alkali intercalation as a predictive synthesis handle analogous to prior work on structure selection by surface stability,[42−44] advancing the field of predictive synthesis and materials design.

METHODOLOGY

To approach the problem of accessing the thermodynamics of the β, γ, R, α, δ, and λ-MnO_2 phases in the presence of alkali intercalation and

DOI: 10.1021/jacs.6b11301
J. Am. Chem. Soc. 2017, 139, 2672−2681

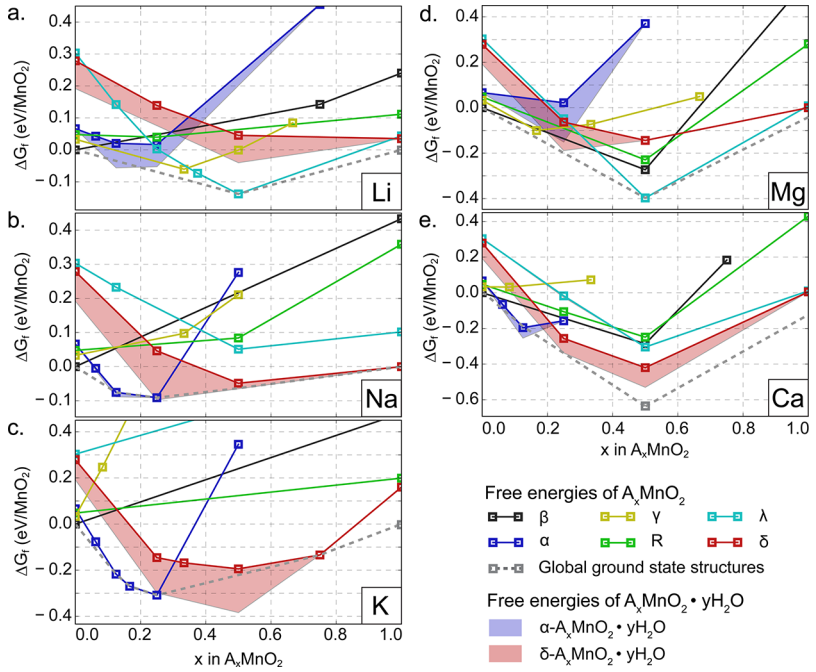

Figure 2. Computed formation free energies of the β, α, R, γ, λ and δ MnO_2 polymorphs intercalated with (a) Li^+, (b) Na^+, (c) K^+, (d) Mg^{2+}, or (e) Ca^{2+} cations. The energy is given with respect to a linear combination of β-MnO_2 and the most stable $AMnO_2$. The solid markers correspond to the ground state structures for a given MnO_2 framework as a function of composition. The dotted line illustrates the global thermodynamic equilibrium along this same composition line, without the restriction that the MnO_2 framework remain topotactic. Finally, the shaded regions depict the range of free energies of each phase that could be expected from hydration, with the lower bound corresponding to equilibrium with pure water at 298 K, assuming that the intercalated water has bulk-like entropy. While all phases were hydrated, only the α and δ phases admitted stable hydrated configurations. Note that the $AMnO_2$ phases for A = Mg, Ca favor the δ phase among the MnO_2 frameworks considered here, but are globally unstable with respect to phase separation into MnO and AO rocksalts.

hydration, we must define a chemical space of interest, determine the structure of all phases across the chemical space, and compare their energetics to that of all competing phases within a grand potential that is representative of the aqueous solutions used in synthesis.

The chemical space we consider are the compounds with the formula $A_xMnO_2{\cdot}yH_2O$ for A = H, Li, Na, K, Mg, Ca, $0 \le x \le 1$, $0 \le y \le 1$, based on the range of intercalation and hydration reported experimentally.[31,45] Within this range, we determine the structure of each of the β, γ, R, α, δ, and λ phases by placing the intercalant cations and/or water in the interstitial sites available in each phase, and choosing the lowest energy structure, as described in the Supporting Information. Furthermore, we map all $A_xMnO_2{\cdot}yH_2O$ phases reported in the Inorganic Crystal Structure Database (ICSD)[45] and the Materials Project[46] to the β, γ, R, α, δ, and λ polymorphs through a distortion-tolerant affine map,[47] or consider them as a competing phase in cases where the underlying MnO_2 framework does not correspond to any of the six polymorphs in question. Through this procedure, we capture all experimentally reported structures, and predict likely low-energy structures within each MnO_2 phase, giving a reliable sample of the configuration space of $A_xMnO_2{\cdot}yH_2O$ compounds.

To obtain accurate energetics for each $A_xMnO_2{\cdot}yH_2O$ structure, we follow the methodology recently established to yield accurate energetics for MnO_2 polymorphs.[10] We perform all DFT calculations within the Vienna Ab Initio Simulation Package (VASP)[48] with projector-augmented wave (PAW) pseudopotentials,[49] a reciprocal space discretization of at least 25 $Å^{-1}$, and the recently introduced SCAN meta-GGA exchange-correlation functional.[40] To balance computational efficiency with accuracy, we prerelax all structures using a Γ-point-only calculation, followed by a pair of full k-point relaxations converged to 2×10^{-7} eV/atom on the electronic structure, and a maximum force of 0.02 eV/Å on all atoms. As the magnetic structure of the Mn sublattice plays a significant role in determining the relative stabilities of MnO_2 polymorphs, we initialize all magnetic configurations using the ground state antiferromagnetic (AFM) orderings given by Kitchaev et al.[10] for structures topotactic to the MnO_2 polymorphs given, or a pair of representative AFM and ferromagnetic (FM) orderings in other cases. To allow for symmetry-breaking relaxations, we do not enforce any symmetry constraints in our calculations. This calculation scheme provides an acceptable balance between accuracy and computational efficiency, although it must be noted that more detailed enumeration and specialized functionals may be needed to reproduce the complex magnetic and charge orderings that arise in some of these phases.[50]

For all structures with alkali and alkali-earth inserted cations, the presence of relatively strong orderings in unhydrated A_xMnO_2 structures limits the contribution of configurational entropy as compared to the enthalpy differences between competing structures. As a result, we can approximate the relative Gibbs free energies of the A_xMnO_2 structures by their DFT-derived $T = 0$ K enthalpies. In the case of proton insertion, this assumption is not necessarily valid, as the interactions between protons in the structure may be insufficient to limit their configurational entropy, and we find that the enthalpy differences between H_xMnO_2 structures are small enough to be competitive with entropic effects. Similarly, the phonon modes associated with the vibrationally active O−H bonds may significantly contribute to the free energies of protonated MnO_2 structures at room temperature. To account for these effects, we bound the contribution of protons to the configurational entropy by that of an ideal lattice solution, based on the lattice defined by protons in the relatively well-ordered MnOOH structures. Furthermore, we calculate the zero-point energy and phonon entropy of all low-enthalpy H_xMnO_2 structures.[51] Put together, the DFT-derived enthalpy, phonon zero-point energy, configurational entropy, and vibrational free energy yield the relative Gibbs free energies of H_xMnO_2 phases. Finally, in the case of hydrated structures, the DFT-calculated formation energy of $A_xMnO_2{\cdot}yH_2O$ from bulk water and A_xMnO_2 formally corresponds to the enthalpy of hydration. While the entropy of the hydration reaction is difficult to calculate exactly, we place a bound on its magnitude by assuming that the intercalated water has an entropy that is no higher than that of

DOI: 10.1021/jacs.6b11301
J. Am. Chem. Soc. 2017, 139, 2672−2681

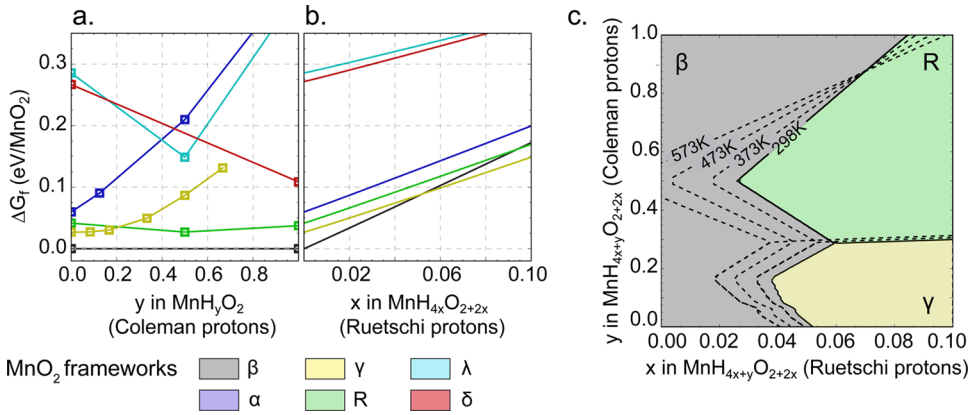

Figure 3. Thermodynamics of proton incorporation into MnO_2 polymorphs, as (a) reducing (Coleman) protons, and (b) nonreducing (Ruetschi) protons. In (a) and (b), the solid lines indicate the formation free energy at each proton concentration with respect to the β-type pyrolusite-manganite equilibrium line (a) or β-MnO_2 and water (b). All formation energies are given at 298 K, accounting for the effect of DFT-derived formation enthalpy, phonon zero-point energy, vibrational free energy, and configurational entropy. (c) The combined effect of Coleman and Ruetschi protons on stabilizing R- and γ-MnO_2 with respect to β, assuming that their effect on the free energy of $MnH_{4x+y}O_{2+2x}$ is independent.

bulk water. While a significant simplification, this bound is sufficient to establish the key effects of hydration on MnO_2 thermodynamics.

On the basis of the calculated energetics, we derive the intercalation phase diagram of each MnO_2 polymorph by constructing the convex hull of all topotactically related structures. Combining these convex hulls, we construct the open-system phase diagrams, which map the equilibrium phases as a function of pH and alkali chemical potential. In the case of phase diagrams given as a function of composition, we calculate formation energies with respect to pure β-MnO_2, the ground state $AMnO_2$ structure, and liquid water at 298 K. In the case of open systems, the zero of alkali chemical potential is chosen as that of the ion at a 1 molal concentration in water at 298 K and pH = 0 at zero applied potential, which we calculate as the DFT energy of the elemental reference plus the experimentally measured formation energy of the alkali ion in water.[52] To partially counteract the effect of electron self-interaction in the Mn *d*-states, we apply a constant potential shift equal to 0.337 V to all calculated structures so as to reproduce the experimental formation energy of β-MnO_2 with respect to Mn and O_2 gas in the open-system phase diagrams. Finally, we use experimentally reported equilibria to set the energy of the hausmannite Mn_3O_4 structure.[53,54] While we must introduce a trade-off between redox potential accuracy and structure prediction accuracy in choosing to use SCAN instead of the more common Hubbard-*U* approach,[52,55] we find our aqueous stability results to be accurate within 2 pH units,[53] which is acceptable for evaluating the structure selection trends we are interested in.

RESULTS

We begin by evaluating the thermodynamics of alkali and alkali-earth intercalation into MnO_2 structures in a dry environment in order to establish the baseline effect of cation type and concentration on the stability of β, α, R, γ, δ, and λ MnO_2 phases. For each of A = Li, Na, K, Mg, and Ca, the formation energy of each polymorph at concentration A_xMnO_2 with respect to phase separation between β-MnO_2 and the ground state $AMnO_2$ structure is given in Figure 2 (this choice of reference state is arbitrary and only serves to clearly present the data here). The solid squares and lines denote the ground states within a constrained MnO_2 framework, i.e., the behavior for the topotactic insertion of A. The gray dashed line denotes the energy of the global equilibrium ground state configuration of A_xMnO_2, without any constraints on the MnO_2 sublattice. As such, the curves in Figure 2 give not only the equilibrium configuration of A_xMnO_2 polymorphs at each composition, but also the driving force for phase transformation between each pair of polymorphs, or other phases non explicitly considered. For example, in the case of Na_xMnO_2, all ground state configurations are commensurate with the MnO_2 polymorphs we consider, while in the case of Ca_xMnO_2, other ICSD-reported structures arise as the ground state across a limited composition range, even along the A_xMnO_2 composition line. Detailed information on the thermodynamic ground states of each polymorph, as well as that of each A_xMnO_2 system as a whole is available as an explorable data set online (https://materialsproject.org/mpcontribs/MnO2_phase_selection/), as a contribution to the Materials Project, as well as in the Supporting Information. With alkali insertion, the lowest energy polymorph changes frequently, and different inserting ions can stabilize different polymorphs, creating a clear opportunity for polymorph selection through the controlled addition of group I or II elements during synthesis.

We proceed from the baseline energetics of the dry A_xMnO_2 structures to consider the effect of hydration on the formation energy of each MnO_2 polymorph. The shaded regions below the equilibrium lines of the α and δ phases in Figure 2 denote the likely range of formation energies for hydrated $A_xMnO_2 \cdot yH_2O$ structures, with the uncertainty in the exact value arising from the fact that we are unable to reliably calculate the entropy of intercalated water, and instead simply bound the entropy by that of bulk water. Note that while we calculate the hydration energy of all polymorphs, only the α and δ phases yield hydrated configurations energetically favorable with respect to the dry A_xMnO_2 structure and bulk water at 298 K. As a result, we do not plot the hydration energies of the β, R, γ or λ structures.

Finally, we evaluate the effect of proton incorporation, where we classify protons by whether or not they lead to the reduction of Mn from 4+ to 3+. Following previous work by Ruetschi et al.,[56] we term protons which intercalate into the structure and reduce Mn as Coleman protons,[57] and those which compensate Mn vacancies and are not involved in redox reactions as Ruetschi protons.[56,58]

The formation energy of Coleman protons, whose thermodynamics are shown in Figure 3a, can be represented analogously to the larger alkali ions as their formation is a type of intercalation reaction. However, as protonated structures form vibrationally active O−H bonds, we also consider the effects of zero-point energy and phonon free energy.

DOI: 10.1021/jacs.6b11301
J. Am. Chem. Soc. 2017, 139, 2672−2681

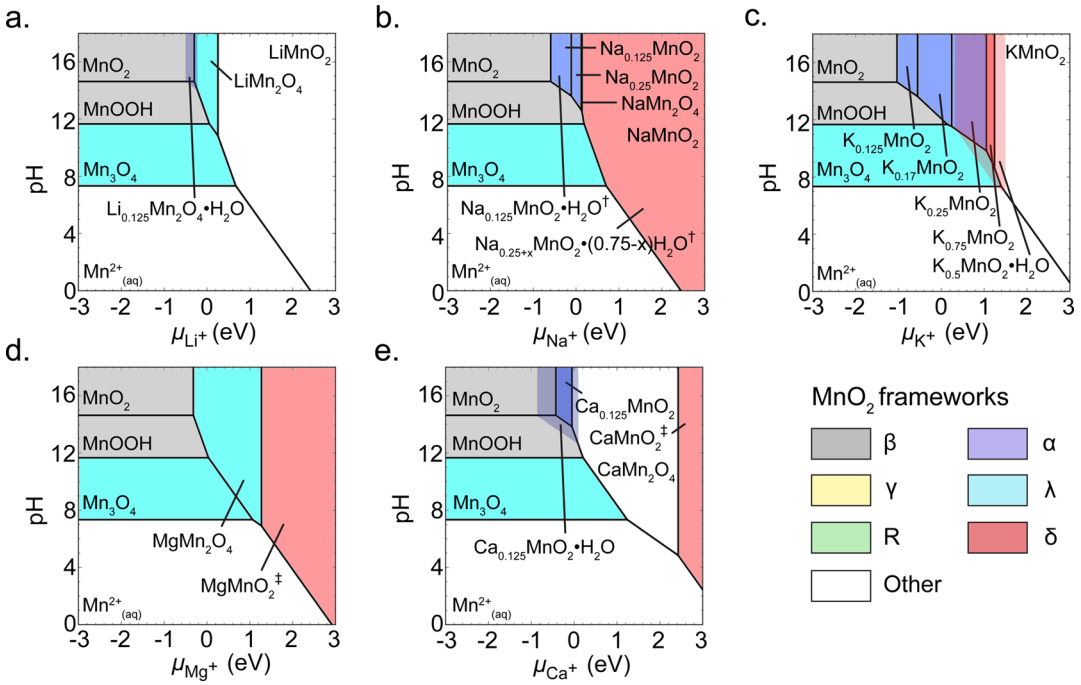

Figure 4. Constrained equilibrium thermodynamics driving phase selection between MnO_2 polymorphs as a function of solution conditions at 298 K and zero applied potential, for solutions containing (a) Li^+, (b) Na^+, (c) K^+, (d) Mg^{2+}, or (e) Ca^{2+} cations. The zero of the alkali-ion chemical potential corresponds to the chemical potential of the ion in an aqueous solution at a 1 molal concentration. The bixbyite Mn_2O_3 phase does not appear here as we find it to be unstable with respect to MnOOH up to 231 °C, in close agreement with TGA experiments[60] and recent DFT results,[55] but in conflict with older results.[61] Hydrated configurations from Figure 2 are included as lightly shaded regions demonstrating the relative stability of hydrated phases but not the precise hydrated composition, which we do not resolve in this study. The set of reactions considered in these phase diagrams are available in the Supporting Information. In particular, we do not include the A_xMnO_{2+y} manganate phases which would appear under oxidizing conditions as they fall outside the scope of our analysis, or the alkali oxides and hydroxides which would appear at high alkali potential. [†]The hydrated α and δ regions align almost exactly with the nonhydrated regions and are not shown for clarity. [‡]The $AMnO_2$ phases for A = Mg, Ca favor the δ phase among the MnO_2 frameworks considered here, but are unstable with respect to phase separation into MnO and AO rocksalts.

Furthermore, as this type of proton is highly mobile,[58] we must account for the contribution of configurational entropy to the formation energy. Thus, in Figure 3a, the solid lines correspond to the Gibbs free energy of formation along the H_xMnO_2 composition line at 298 K, estimated from the sum of the DFT-derived enthalpy of formation, the phonon zero point energy, vibrational free energy, and configurational entropy. More detailed free energy curves of MnO_2 and MnOOH structures are available in the Supporting Information. Interestingly, we find the contribution of zero-point energy and vibrational free energy to the relative stability of MnO_2 polymorphs is minimal. This result is likely due to the fact that the local bonding environment in all phases is very similar, making finite temperature vibrational effects a weak handle for polymorph selection.

In contrast to Coleman protons, which can be thermodynamically stabilized by controlling the external chemical potential of H^+, Ruetschi protons are equivalent to structural water and are independent of pH, at least at equilibrium. Thus, the formation energies of Ruetschi protons, shown in Figure 3b for each polymorph with respect to β-MnO_2 and bulk water at 298 K, follow the thermodynamics of isolated point defects. Ruetschi protons exist as localized clusters of four OH^- groups at the site of a Mn^{4+} vacancy, and as such are electrostatically neutral away from the immediate environment of the Ruetschi defect and largely immobile at lower temperatures.[58] As a result, we assume their configurational entropy to be given by the formation entropy of the initial Mn^{4+} vacancy, and the defects to be noninteracting within the 0−10% concentration range shown in Figure 3b. Furthermore, we assume that the effect of O−H vibration within the Ruetschi defects is largely independent of the surrounding structure, affecting their stability versus water but not their relative stability within the various MnO_2 polymorphs. Put together, we find Ruetschi defect formation to be unfavorable at any significant concentration in all MnO_2 structures, but less so in the R and γ phases than β.

In real protonated manganese dioxide structures, both Coleman and Ruetschi protons are reported to be present,[56,59] such that their effect on the formation energy must be considered in tandem. Assuming that the effects of Coleman and Ruetschi protons are approximately independent, we calculate the stability of MnO_2 frameworks across $MnH_{4x+y}O_{2+2x}$ compositions, where x denotes the concentration of Ruetschi defects and y denotes the concentration of Coleman protons. The resulting stability map, given in Figure 3c, reveals that the balance between overall proton content, and the degree to which protons reduce Mn^{4+} determines the relative stability of the β, R, and γ MnO_2 frameworks. While Ruetschi defects, requiring a high activity of H_2O, stabilize the γ phase, the combination of high water content and high acidity, leading to Coleman protons, should help the formation of ramsdellite. Indeed, both the γ and ramsdellite phases are typically grown by plating out of aqueous solution with high acidity.[25]

DOI: 10.1021/jacs.6b11301
J. Am. Chem. Soc. 2017, 139, 2672−2681

Finally, as our primary goal is the control over MnO_2 framework structure during aqueous synthesis, we evaluate the stability of all A_xMnO_2 ground states across a range of solution conditions. Combining the thermodynamic equilibria data given in Figure 2 and Figure 3a, we construct the open-system aqueous phase diagrams for each A_xMnO_2 system, shown in Figure 4. A list of all reactions we consider in this stability map is available in the Supporting Information. To illustrate the effect of hydration on these phase diagrams, we separate the stability regions of unhydrated A_xMnO_2 phases and those of the hydrated α and δ phases. Since we find Ruetschi defects to be unstable with respect to dehydration, we do not include them in these grand-potential equilibrium phase diagrams. Finally, we do not include cointercalated structures, or alkali-rich structures such as the alkali manganates with the formula A_xMnO_{2+y} as they fall outside the scope of the structural and chemical space we are considering, although outside of mild aqueous conditions, in particular at high alkali potentials and in oxidizing environments, these structures do become stable. The aqueous phase diagrams shown in Figure 4 show both the equilibrium compositions of A_xMnO_2 that could be expected to form under various conditions of pH and alkali chemical potential, and the underlying MnO_2 framework, offering a direct comparison to aqueous precipitation experiments reported as synthesis routes for MnO_2 polymorphs. Similarly, these data elucidate the effect of changing solution pH and chemical potential on alkali stability within MnO_2 frameworks, giving a quantitative map for the acid-induced chemical extraction of alkali ions from MnO_2 frameworks, and the corresponding phase transformations.[24]

DISCUSSION

Alkali-Stabilized Phases: α, λ, and δ. The first conclusion we are able to draw from our analysis is that the α, λ, and δ frameworks, while not the ground states for the MnO_2 composition, are thermodynamically stabilized by alkali intercalation, meaning that control over the product MnO_2 framework can be achieved by controlling the chemical potential of alkali cations in the precursor solution. Specifically, Li^+ and Mg^{2+} favor the spinel (λ) phase, Na^+, Ca^{2+}, and especially K^+ favor the hollandite (α) phase, and all cations except Li^+ favor the layered (δ) phase in some composition range. During hydrothermal growth, these cations are typically present in the growth solution either from a MnO_4^- precursor salt, or as a deliberate additive (typically, as an alkali hydroxide salt). As a result, the primary handle over alkali chemical potential is the initial salt concentration, leading to β, α, λ, or δ-type A_xMnO_2 growth. This result is consistent with a number of reported transitions between MnO_2 frameworks. For example, several experimental studies report a transition from β to α to δ on increasing the K^+ content in the precursor solution, and the reverse transformation with decreasing pH.[23,24,62−64] These observations are in qualitative agreement with the phase diagram shown in Figure 4c, although it is difficult to compare the results quantitatively as the authors do not maintain a consistent K^+ concentration in the solution throughout the synthesis, or consistently report the pH for their reactions.

We can further validate our results indirectly based on reported phase transformations during the electrochemical cycling of alkali-containing MnO_2 structures. For example, the decomposition of the orthorhombic $LiMnO_2$ structure to the λ-type $LiMn_2O_4$ spinel on Li^+ removal which can be seen in Figure 4a is well documented in the literature.[65,66] Similarly, Sun et al. have recently reported that Mg^{2+} intercalation into δ-MnO_2 in the absence of water results in irreversible decomposition of the δ structure, while in the presence of water, quasireversible conversion between hydrated δ-$Mg_{0.15}MnO_2{\cdot}0.9H_2O$ and dry λ-MnO_2 is possible.[28] This result is in agreement with the stabilization of δ-$Mg_{0.25}MnO_2$ by hydration seen in Figure 2d with respect to the anhydrous β-MnO_2−λ-$Mg_{0.5}MnO_2$ equilibrium line. As the anhydrous δ phase is never stable for Mg_xMnO_2, $0 \le x \le 0.5$, we would expect that after initial decomposition on Mg insertion, there would never be a driving force for the δ phase to reform on Mg extraction, while in the hydrated case, reformation of the δ structure is thermodynamically plausible. The coupling between intercalation and structure selection seen in our data, and illustrated in these experiments, enables electrochemical processing to function as an effective structure-sensitive synthesis tool in the case of redox-active systems such as MnO_2.

The mechanism by which various alkali cations stabilize a particular polymorph is related to two primary characteristics of a MnO_2 framework—the compatibility between available interstitial sites and the preferred coordination environment of the alkali ion, and the ability of the framework structure to accommodate changes in electronic configuration, both due the electrostatic repulsion of intercalated cations, and the change in Mn redox state upon intercalation. To derive these characteristics, we examine the effect of cation size and cation valence, noting that Li^+ and Mg^{2+} have very similar ionic radii, as do Na^+ and Ca^{2+}, which allows us to examine the effects of size and valency independently of each other. Furthermore, we relate the stabilization of certain A_xMnO_2 structures by water to the ability of water to increase the coordination of cations in otherwise unstable sites, creating a partial solvation shell around around the cation. Importantly, structure stabilization by water is specifically not a consequence of the interaction of water with the MnO_2 framework directly, but rather of the ability of water to stabilize intercalated cations in the structure.

The first relationship between cation type and phase selection is that of the compatibility between available interstitial sites in the structure and the preferred coordination of the alkali ion. For example, the hollandite α phase contains four potential intercalation sites—the 8-fold coordinated 2b and 4-fold coordinated 2a tunnel-centered sites, and the asymmetrically 4-fold and 5-fold coordinated off-center 8h′ and 8h sites, respectively. The only cation large enough to occupy the 2b site is K^+, creating a highly stable, well-coordinated alkali-oxygen environment that results in the wide window of stability for α-MnO_2 across K^+ chemical potentials consistent with experimental results.[23,24,62−64] The slightly smaller Na^+ and Ca^{2+} are not stable in the 2b site, instead occupying the lower-coordinated 2a and 8h sites. Nonetheless, the bonding afforded by these sites, while less strong than in the case of K^+, provides sufficient alkali-oxygen coordination to stabilize α within a limited range of Na^+ and Ca^{2+} chemical potentials. Finally, in the case of Li^+ and Mg^{2+}, the ionic radius of the cation is only compatible with the asymmetric and low-coordinated 8h and 8h′ sites, failing to provide any reasonable coordination geometry for the intercalated cations. Thus, Li^+ and Mg^{2+} do not stabilize the α framework in agreement with reported decomposition of the α phase on Li^+ and Mg^{2+} insertion.[3,39]

The opposite trend can be observed in the stability of the λ phase, which only has relatively small tetrahedral and

DOI: 10.1021/jacs.6b11301
J. Am. Chem. Soc. 2017, 139, 2672−2681

octahedral sites. The small alkali-oxygen bond lengths of the tetrahedral site allow it to form a highly stable coordination environment in the presence of Li^+ or Mg^{2+}, while failing to accommodate the larger Na^+, Ca^{2+}, or especially K^+ ions, as can be seen by the destabilization of the tetrahedrally occupied spinel-type λ-AMn_2O_4 with increasing cation size. However, the most extreme example of coordination preference is that of proton-incorporated structures. While intercalated protons tightly bind to oxygen to form OH^- groups, stable proton sites are those where the proton bridges two oxygens, in agreement with previous FTIR results.[67] The $[1 \times 1]$ and $[2 \times 1]$ tunnels in β, R and γ, as well as the layer stacking arrangement in δ, create numerous environments where such a O−H−O bridge is possible, while the $[2 \times 2]$ tunnel structure of α does not allow for any such environments to form. Correspondingly, the α phase is rapidly destabilized by proton intercalation, as can be seen in Figure 3a. Thus, compatibility of cation size and coordination preference with the MnO_2 framework is a key parameter determining the feasibility of structural stabilization by alkali intercalation.

A second characteristic of alkali-to-polymorph compatibility is the ability of the transition metal structure to accommodate the valency of the alkali, manifested both in reduction of the transition metal, and the electrostatic repulsion between the intercalants. A clear example of this effect is the difference in the stabilization of α by the similarly sized Na^+ and Ca^{2+}, seen in Figures 2b and 2e. While both cations occupy similar 2a and 8h sites, the maximum stable concentration of Ca^{2+} in the α tunnels is lower than that of Na^+ due to the stronger electrostatic repulsion between Ca^{2+} ions in the same α tunnel. As a result, the composition window over which Na^+ stabilizes α is much wider, as can be seen in Figure 2.

The effect of transition metal redox can be most clearly seen in the differences in phase selection between Li^+ and Mg^{2+}. At the fully intercalated $AMnO_2$ composition, all low energy structures place the alkali ion into an octahedral site, with the key difference that in the Li case, the Mn is in the Jahn−Teller active Mn^{3+} redox state, while in the Mg case, the Mn is in the Jahn−Teller inactive Mn^{2+} state. As a result, the structure of $MgMnO_2$ is the highly symmetric O3-δ phase, with the similarly symmetric octahedrally occupied λ only slightly unstable, while the $LiMnO_2$ structure strongly favors the low-symmetry o-$LiMnO_2$ geometry, which is able to accommodate Jahn−Teller distortions much better than the δ or λ phases. A similar effect can be seen in the Na^+ and Ca^{2+} cases at the AMn_2O_4 composition. In the $CaMn_2O_4$ case, the Mn is fully in the Jahn−Teller active 3+ state, while in the $NaMn_2O_4$ case, half of the Mn remains in the Jahn−Teller inactive 4+ state. Correspondingly, Ca^{2+} stabilizes the highly distorted marokite-type structure, while $NaMn_2O_4$ exists in the more symmetric postspinel phase. A detailed illustration of the Jahn−Teller distortions in Mn^{3+}-containing structures as compared to Mn^{2+} and Mn^{4+} phases, which we calculate in close agreement with recent EXAFS results,[68] is available in Supplementary Figure S3. While neither of these structures correspond to the six canonical MnO_2 polymorphs, they provide further evidence to the relationship between redox-state-controlled coordination-environment distortions and phase selection. Put together, the need for the transition-metal framework to accommodate both the change in the transition-metal redox state, and minimize electrostatic repulsion between intercalants introduces a further degree of selectivity between intercalant and the polymorphs it is able to stabilize.

The last important characteristic of alkali-mediated phase stabilization is the interaction of intercalated phases and water, analogous to recently reported results in MgV_2O_5.[69] In pure MnO_2 structures, the only phase that we predict to hydrate exothermically is the layered δ phase, with even the fairly open α phase preferring to dehydrate. These results are consistent with the relaxed structure of the hydrated phases—while the hydrated structures are initialized with many water molecules oriented so as to create proton bridges with the oxygens in the MnO_2 framework, relaxed hydrated structures always minimize bonding between MnO_2 and water, creating clusters of water molecules that appear to be repelled from the MnO_2 structure itself. Similar structural changes occur in δ also, but it is likely that the medium-range van-der-Waals interactions with the water layer are stronger than between MnO_2 layers, stabilizing hydration even in the absence of direct bonding between MnO_2 and water.

In the presence of alkali cations, the behavior of water in the structures changes dramatically, as water is now able to bind to the highly soluble alkali cations. As discussed earlier, the Li^+ and Mg^{2+}-intercalated α phase is unstable due to the low coordination of the alkali cations. When these structures are hydrated up to 0.25 mol H_2O/mol MnO_2, however, the water coordinates the cations so as to increase their coordination from 4- and 5-fold for Li^+ and Mg^{2+} to 6-fold and 7-fold, respectively. As the water compensates the undercoordination with a partial solvation shell, hydration helps to stabilize the intercalated α phase, as can be seen in Figures 2a and 2d. Conversely, in the relatively well-coordinated Na^+ and Ca^{2+} α phases, hydration has a negligible effect on phase stability, while in the well-coordinated K-intercalated α, hydration is endothermic even at dilute K content. Thus, we may conclude that the most important effect of water is to stabilize alkali cations in otherwise unstable, undercoordinated environments, helping stabilize less dense MnO_2 frameworks. While we did not consider larger tunnel structures in this work, it is possible that this stabilization of undercoordinated alkali intercalants by water may explain the success of synthesis recipes for the larger $[2 \times 3]$, $[2 \times 4]$ and $[3 \times 3]$ tunnel analogues of the α phase by the cointercalation of significant quantities of Na^+ and water.[70−73] Similarly, the energetic balance of alkali coordination by the MnO_2 framework and cointercalated water explains the diversity of birnessite and buserite minerals, all variants of the layered δ phase with varying degrees of alkali solvation.[74,75]

Proton-Stabilized Phases: γ and R. While alkali intercalation explains the stability of α, δ, and λ-MnO_2, the two remaining frameworks, R and γ, are never ground states for any level of alkali incorporation. In the case of Li^+ and Mg^{2+}, the formation energy of R and γ with respect to the true thermodynamic ground state is small, as can be seen in Figures 2a and 2d, which is consistent with experimental reports of metastable R- and γ-type Li_xMnO_2.[22] Nonetheless, it does not appear that any level of lithiation can truly thermodynamically stabilize the R or γ type framework.

We may speculate that one possible mechanism explaining the formation of ramsdellite is based on the effect of Coleman protons and the contribution of their configurational entropy to free energy at relatively high temperatures. On the basis of the stability map shown in Figure 3c, one route by which R-MnO_2 could form is through the entropically stabilized R-type $H_{0.5}MnO_2$. Indeed, a R-type phase at this composition has been previously observed as a transient state in ramsdellite growth, as well as proton insertion into ramsdellite.[12,76] In both

DOI: 10.1021/jacs.6b11301
J. Am. Chem. Soc. 2017, 139, 2672−2681

cases, this phase has been termed "groutellite" by analogy to the metastable R-type groutite MnOOH phase. Single-crystal ramsdellite can be synthesized through hydrothermal processing of a Li_xMnO_2 precursor in strong acid,[9,22] which further suggests that acid-mediated delithiation may lead to the formation of a protonated intermediate, which at high temperatures would favor the R-MnO_2 framework. The incorporation of protons into MnO_2 frameworks during acid-induced ion extraction may be key to the formation of the relatively dense R-MnO_2 structure, which much like β, is too dense to be stabilized by the intercalation of significant quantities of any cation larger than H^+.

One alternate mechanism for the formation of the R and γ phases involves the formation of Ruetschi defects. While these defects are metastable, and have been shown to irreversibly anneal out of the structure,[56] Ruetschi defects are typically present in electrolytic manganese oxide (EMD), which predominantly consists of the γ phase.[12] The typical concentration of Ruetschi defects found in EMD is 5−9 mol %,[56,59] at which composition we indeed find γ or R to be the stable form of MnO_2 based on the stability map in Figure 3c. We may speculate that the origin of the trapped protons is twofold. First, as EMD is typically grown by electrodeposition at high rates from an acidic solution of $MnSO_4$ and H_2SO_4,[25] the deposition of MnO_2 solid from Mn^{2+} ions involves the deprotonation of H_2O.[77] At high deposition rates, any incomplete deprotonation would lead to a fraction of hydroxyl groups in the deposited structure, which would lead to the formation of Ruetschi defects, or metastable Coleman protons. After they are formed, however, it is very difficult for Ruetschi defects to anneal out of the structure. To do so, they must reform a water molecule, which then must be transported through the EMD bulk. However, the $[2 \times 1]$ and $[1 \times 1]$ tunnels making up the γ-MnO_2 structure are small, such that the activation barrier for water to diffuse through the structure is very high, based on the energy required to place a water molecule in a R or γ-phase tunnel. Consequently, after their initial formation, Ruetschi defects likely remain trapped in the EMD structure, thereby stabilizing it against transformation to the β ground state phase.

Put together, the Ruetschi defects and Coleman protons may both stabilize R and γ, as can be seen in Figure 3c. Thus, while the two mechanisms are distinct and are likely to arise in differing synthesis environments, both can lead to the formation of R or γ, suggesting that the careful characterization of proton content in MnO_2 may reveal the formation mechanisms for these two phases.

Circumstantial evidence of the importance of protons in the formation of R and γ can be found in existing *in situ* data. Shen et al.[29] observe a series of transformations from Na-birnessite precursors to other MnO_2 phases by *in situ* diffraction. The first observed pathway, which forms β from the birnessite precursor at high temperature and in highly acidic media, involves initial layer collapse due to chemical desodiation and/or dehydration, followed by a transformation from δ to R/γ and eventually β. It is likely that the acid-induced chemical desodiation of the structure simultaneously destabilizes the δ-MnO_2 framework, as can be seen in Figure 2b, and leads to the incorporation of protons into the MnO_2 structure. The proton incorporation leads to the formation of R/γ-MnO_2 at high temperature, which transforms to the β ground state as the protons are slowly annealed out. Consistent with this interpretation, the authors observe a change of the end point phase from β to α and a disappearance of the R/γ intermediate when the reaction is done in a more basic environment and at a higher external sodium chemical potential. While alternate explanations of these observed pathways are certainly possible, we hypothesize that this quasiequilibrium thermodynamic interpretation of the generally slow transformation process provides a compelling energetic foundation for phase transformations such as that reported by Shen et al. in this system.

CONCLUSION

The predictive design of synthesis recipes targeting specific polymorphs of compounds is a key challenge for materials design.[78] We have investigated the coupling between intercalation reactions and structure selection during MnO_2 synthesis, focusing in particular on the β, α, R, γ, δ, and λ polymorphs of MnO_2, synthesized from alkali and alkali-earth containing aqueous solutions. We have identified the compositions and solution conditions that could be expected to stabilize each of the common MnO_2 frameworks, and identified likely mechanisms leading to the formation of these polymorphs. Specifically, the α phase is stabilized by Na^+, Ca^{2+}, K^+ and hydration due to its ability to highly coordinate cations with framework oxygens or inserted H_2O. The λ phase is stabilized by Li^+ and Mg^{2+}, which prefer the small, low coordination sites in this structure. The δ phase is stabilized by hydration and in particular Na^+. To explain these results, we have highlighted the key importance of (1) the compatibility between available interstitial sites and cation bonding preference, (2) the ability of the transition metal framework to accommodate the valency of the intercalant, and (3) the ability of water to form a partial solvation shell around the intercalated alkali, on the stabilization of MnO_2 frameworks by alkali intercalation. Finally, we identified (4) the key importance of protons in the formation of the R and γ forms of MnO_2, both during hydrothermal processing and electrochemical deposition. Our work establishes a self-consistent thermodynamic baseline for the stability of MnO_2 polymorphs that will facilitate the quantitative prediction of synthesis outcomes in this system and the interpretation of phase transformation data, and contribute to the development of functional manganese oxide materials. More generally, our open system *ab initio* approach is directly applicable to understanding synthesis in other chemical spaces.

ASSOCIATED CONTENT

Supporting Information

The Supporting Information is available free of charge on the ACS Publications website at DOI: 10.1021/jacs.6b11301.

Generation of A_xMnO_2 intercalated structures; Hydration; Generation of Ruetschi defects; Derivation of aqueous chemical equilibria; Thermal effects in MnO_2 and MnOOH structures; Jahn−Teller distortions in Mn^{3+} compounds; Energies of constrained-equilibrium structures (PDF)

AUTHOR INFORMATION

Corresponding Authors

*E-mail: dkitch@mit.edu.

*E-mail: gceder@berkeley.edu.

ORCID

Daniil A. Kitchaev: 0000-0003-2309-3644

Stephen T. Dacek: 0000-0002-7737-1278

DOI: 10.1021/jacs.6b11301
J. Am. Chem. Soc. 2017, 139, 2672−2681

Author Contributions

[§]S.T.D. and W.S. contributed equally.

Notes

The authors declare no competing financial interest.

■ ACKNOWLEDGMENTS

The authors of this work would like to thank Patrick Huck for assistance with the Materials Project infrastructure. This work was supported by the Center for Next-Generation of Materials by Design, an Energy Frontier Research Center funded by U.S. Department of Energy, Office of Basic Energy Science. Data dissemination through the Materials Project was supported by the NSF Software Infrastructure for Sustained Innovation (SI2-SSI) Collaborative Research program of the National Science Foundation under Award No. OCI-1147503. Computational resources for this project were provided by the National Energy Research Scientific Computing Center, a DOE Office of Science User Facility supported by the Office of Science of the U.S. Department of Energy under Contract No. DE-AC02-05CH11231.

■ REFERENCES

(1) Jain, A.; Shin, Y.; Persson, K. A. *Nat. Rev. Mater.* **2016**, *1*, 15004.
(2) Tarascon, J. M. *J. Electrochem. Soc.* **1991**, *138*, 2859.
(3) Thackeray, M. M. *Prog. Solid State Chem.* **1997**, *25*, 1−71.
(4) Bergmann, A.; Zaharieva, I.; Dau, H.; Strasser, P. *Energy Environ. Sci.* **2013**, *6*, 2745−2755.
(5) Huynh, M.; Shi, C.; Billinge, S. J. L.; Nocera, D. G. *J. Am. Chem. Soc.* **2015**, *137*, 14887−904.
(6) Suib, S. L. *Acc. Chem. Res.* **2008**, *41*, 479−487.
(7) Wei, W.; Cui, X.; Chen, W.; Ivey, D. G. *Chem. Soc. Rev.* **2011**, *40*, 1697−1721.
(8) Post, J. E. *Proc. Natl. Acad. Sci. U. S. A.* **1999**, *96*, 3447−3454.
(9) Robinson, D. M.; Go, Y. B.; Mui, M.; Gardner, G.; Zhang, Z.; Mastrogiovanni, D.; Garfunkel, E.; Li, J.; Greenblatt, M.; Dismukes, G. C. *J. Am. Chem. Soc.* **2013**, *135*, 3494−3501.
(10) Kitchaev, D. A.; Peng, H.; Liu, Y.; Sun, J.; Perdew, J. P.; Ceder, G. *Phys. Rev. B: Condens. Matter Mater. Phys.* **2016**, *93*, 045132.
(11) Delmas, C.; Fouassier, C.; Hagenmuller, P. *Physica B+C* **1980**, *99*, 81−85.
(12) Chabre, Y.; Pannetier, J. *Prog. Solid State Chem.* **1995**, *23*, 1−130.
(13) Hill, L.; Verbaere, A. *J. Solid State Chem.* **2004**, *177*, 4706−4723.
(14) Zhu, H. T.; Luo, J.; Yang, H. X.; Liang, J. K.; Rao, G. H.; Li, J. B.; Du, Z. M. *J. Phys. Chem. C* **2008**, *112*, 17089−17094.
(15) Tompsett, D. A.; Middlemiss, D. S.; Islam, M. S. *Phys. Rev. B: Condens. Matter Mater. Phys.* **2012**, *86*, 205126.
(16) Crespo, Y.; Seriani, N. *Phys. Rev. B: Condens. Matter Mater. Phys.* **2013**, *88*, 144428.
(17) Yoshimori, A. *J. Phys. Soc. Jpn.* **1959**, *14*, 807−821.
(18) Greedan, J. E.; Raju, N. P.; Wills, A. S.; Morin, C.; Shaw, S. M.; Reimers, J. N. *Chem. Mater.* **1998**, *10*, 3058−3067.
(19) Hunter, J. C. *J. Solid State Chem.* **1981**, *39*, 142−147.
(20) Clearfield, A. *Chem. Rev.* **1988**, *88*, 125−148.
(21) Rossouw, M.; Liles, D.; Thackeray, M.; David, W.; Hull, S. *Mater. Res. Bull.* **1992**, *27*, 221−230.
(22) Thackeray, M.; Rossouw, M.; Gummow, R.; Liles, D.; Pearce, K.; Kock, A. D.; David, W.; Hull, S. *Electrochim. Acta* **1993**, *38*, 1259−1267.
(23) DeGuzman, R. N.; Shen, Y.-F.; Neth, E. J.; Suib, S. L.; O'Young, C.-L.; Levine, S.; Newsam, J. M. *Chem. Mater.* **1994**, *6*, 815−821.
(24) Portehault, D.; Cassaignon, S.; Baudrin, E.; Jolivet, J.-P. *J. Mater. Chem.* **2009**, *19*, 2407.
(25) Sarciaux, S.; Salle, A. L. G. L.; Verbaere, A.; Piffard, Y.; Guyomard, D. *J. Power Sources* **1999**, *81−82*, 656−660.
(26) Lv, D.; Huang, X.; Yue, H.; Yang, Y. *J. Electrochem. Soc.* **2009**, *156*, A911−A916.
(27) Ma, X.; Chen, H.; Ceder, G. *J. Electrochem. Soc.* **2011**, *158*, A1307−A1312.
(28) Sun, X.; Duffort, V.; Mehdi, B. L.; Browning, N. D.; Nazar, L. F. *Chem. Mater.* **2016**, *28*, 534−542.
(29) Shen, X.-F.; Ding, Y.-S.; Hanson, J. C.; Aindow, M.; Suib, S. L. *J. Am. Chem. Soc.* **2006**, *128*, 4570−4571.
(30) Birgisson, S.; Jensen, K. M. O.; Christiansen, T. L.; von Bulow, J. F.; Iversen, B. B. *Dalton Trans.* **2014**, *43*, 15075−15084.
(31) Fritsch, S.; Post, J. E.; Suib, S. L.; Navrotsky, A. *Chem. Mater.* **1998**, *10*, 474−479.
(32) Tiana, Z.-R.; Xia, G.; Luo, J.; Suib, S. L.; Navrotsky, A. *J. Phys. Chem. B* **2000**, *104*, 5035−5039.
(33) Reed, J.; Ceder, G.; Van Der Ven, A. *Electrochem. Solid-State Lett.* **2001**, *4*, A78−A81.
(34) Balachandran, D.; Morgan, D.; Ceder, G.; van de Walle, A. *J. Solid State Chem.* **2003**, *173*, 462−475.
(35) Cockayne, E.; Li, L. *Chem. Phys. Lett.* **2012**, *544*, 53−58.
(36) Wei, Z.-g.; Yan, J.-h.; Wu, Y.; Liu, Y. *Chin. J. Chem. Phys.* **2015**, *28*, 711−715.
(37) Tompsett, D. A.; Islam, M. S. *Chem. Mater.* **2013**, *25*, 2515−2526.
(38) Wang, D.; Liu, L.-M.; Zhao, S.-J.; Li, B.-H.; Liu, H.; Lang, X.-F. *Phys. Chem. Chem. Phys.* **2013**, *15*, 9075−83.
(39) Ling, C.; Zhang, R.; Arthur, T. S.; Mizuno, F. *Chem. Mater.* **2015**, *27*, 5799−5807.
(40) Sun, J.; Ruzsinszky, A.; Perdew, J. P. *Phys. Rev. Lett.* **2015**, *115*, 036402.
(41) De Yoreo, J. J.; Gilbert, P. U.; Sommerdijk, N. A.; Penn, R. L.; Whitelam, S.; Joester, D.; Zhang, H.; Rimer, J. D.; Navrotsky, A.; Banfield, A. F.; Wallace, J. F.; Michel, F. M.; Meldrum, F. C.; Colfen, H.; Dove, P. M. *Science* **2015**, *349*, aaa6760.
(42) Navrotsky, A. *Geochem. Trans.* **2003**, *4*, 1−4.
(43) Sun, W.; Jayaraman, S.; Chen, W.; Persson, K. A.; Ceder, G. *Proc. Natl. Acad. Sci. U. S. A.* **2015**, *112*, 3199−3204.
(44) Kitchaev, D. A.; Ceder, G. *Nat. Commun.* **2016**, *7*, 13799.
(45) Belsky, A.; Hellenbrandt, M.; Karen, V. L.; Luksch, P. *Acta Crystallogr., Sect. B: Struct. Sci.* **2002**, *58*, 364−369.
(46) Jain, A.; Ong, S. P.; Hautier, G.; Chen, W.; Richards, W. D.; Dacek, S.; Cholia, S.; Gunter, D.; Skinner, D.; Ceder, G.; Persson, K. a. *APL Mater.* **2013**, *1*, 011002.
(47) Ong, S. P.; Richards, W. D.; Jain, A.; Hautier, G.; Kocher, M.; Cholia, S.; Gunter, D.; Chevrier, V. L.; Persson, K. A.; Ceder, G. *Comput. Mater. Sci.* **2013**, *68*, 314−319.
(48) Kresse, G.; Furthmüller, J. *Comput. Mater. Sci.* **1996**, *6*, 15−50.
(49) Kresse, G.; Joubert, D. *Phys. Rev. B: Condens. Matter Mater. Phys.* **1999**, *59*, 1758−1775.
(50) Li, X.; Ma, X.; Su, D.; Liu, L.; Chisnell, R.; Ong, S. P.; Chen, H.; Toumar, A.; Idrobo, J.-C.; Lei, Y.; Bai, J.; Wang, F.; Lynn, J. W.; Lee, Y. S.; Ceder, G. *Nat. Mater.* **2014**, *13*, 586−592.
(51) Togo, A.; Tanaka, I. *Scr. Mater.* **2015**, *108*, 1−5.
(52) Persson, K. A.; Waldwick, B.; Lazic, P.; Ceder, G. *Phys. Rev. B: Condens. Matter Mater. Phys.* **2012**, *85*, 235438.
(53) Pourbaix, M. *Atlas of Electrochemical Equilibria in Aqueous Solutions*; National Association of Corrosion Engineers: Houston, TX, 1974.
(54) Birkner, N.; Navrotsky, A. *Am. Mineral.* **2012**, *97*, 1291−1298.
(55) Zeng, Z.; Chan, M. K. Y.; Zhao, Z.-J.; Kubal, J.; Fan, D.; Greeley, J. *J. Phys. Chem. C* **2015**, *119*, 18177−18187.
(56) Ruetschi, P. *J. Electrochem. Soc.* **1984**, *131*, 2737−2744.
(57) Coleman, J. J. *Trans. Electrochem. Soc.* **1946**, *90*, 545−583.
(58) Ruetschi, P.; Giovanoli, R. *J. Electrochem. Soc.* **1988**, *135*, 2663−2669.
(59) Donne, S. W.; Feddrix, F. H.; Glöckner, R.; Marion, S.; Norby, T. *Solid State Ionics* **2002**, *152−153*, 695−701.
(60) Sharma, P. K.; Whittingham, M. *Mater. Lett.* **2001**, *48*, 319−323.

DOI: 10.1021/jacs.6b11301
J. Am. Chem. Soc. 2017, 139, 2672−2681

(61) Hem, J. D. *Chemical Equilibria and Rates of Manganese Oxidation*; Geological Survey Water Supply Paper 1667-A; United States Government Printing Office: Washington, D.C., 1963.
(62) Huang, X.; Lv, D.; Yue, H.; Attia, A.; Yang, Y. *Nanotechnology* **2008**, *19*, 225606.
(63) Duan, X.; Yang, J.; Gao, H.; Ma, J.; Jiao, L.; Zheng, W. *CrystEngComm* **2012**, *14*, 4196−4204.
(64) Yin, B.; Zhang, S.; Jiang, H.; Qu, F.; Wu, X. *J. Mater. Chem. A* **2015**, *3*, 5722−5729.
(65) Jang, Y.; Huang, B.; Wang, H.; Sadoway, D. R.; Chiang, Y. *J. Electrochem. Soc.* **1999**, *146*, 3217−3223.
(66) Idemoto, Y.; Mochizuki, T.; Ui, K.; Koura, N. *J. Electrochem. Soc.* **2006**, *153*, A418−A424.
(67) Kohler, T.; Armbruster, T.; Libowitzky, E. *J. Solid State Chem.* **1997**, *133*, 486−500.
(68) Mattioli, G.; Zaharieva, I.; Dau, H.; Guidoni, L. *J. Am. Chem. Soc.* **2015**, *137*, 10254−10267.
(69) Gautam, G. S.; Canepa, P.; Richards, W. D.; Malik, R.; Ceder, G. *Nano Lett.* **2016**, *16*, 2426−2431.
(70) Golden, D. C.; Chen, C.-C.; Dixon, J. B. *Science* **1986**, *231*, 717−719.
(71) Feng, Q.; Horiuchi, T.; Liu, L.; Yanagisawa, K.; Mitsushio, T. *Chem. Lett.* **2000**, *29*, 284−285.
(72) Xia, G.-G.; Tong, W.; Tolentino, E. N.; Duan, N.-G.; Brock, S. L.; Wang, J.-Y.; Suib, S. L.; Ressler, T. *Chem. Mater.* **2001**, *13*, 1585−1592.
(73) Shen, X.-F.; Ding, Y.-S.; Liu, J.; Cai, J.; Laubernds, K.; Zerger, R.; Vasiliev, A.; Aindow, M.; Suib, S. *Adv. Mater.* **2005**, *17*, 805−809.
(74) Luo, J.; Zhang, Q.; Huang, A.; Giraldo, O.; Suib, S. L. *Inorg. Chem.* **1999**, *38*, 6106−6113.
(75) Wiechen, M.; Zaharieva, I.; Dau, H.; Kurz, P. *Chem. Sci.* **2012**, *3*, 2330−2339.
(76) Post, J. E.; Heaney, P. J. *Am. Mineral.* **2004**, *89*, 969−975.
(77) Clarke, C. J.; Browning, G. J.; Donne, S. W. *Electrochim. Acta* **2006**, *51*, 5773−5784.
(78) Lewis, N. S.; Crabtree, G.; Nozik, A.; Wasielewski, M.; Alivisatos, P. *Basic Research Needs for Solar Energy Utilization*; U.S. Department of Energy, 2005; http://science.energy.gov/~/media/bes/pdf/reports/files/Basic_Research_Needs_for_Solar_Energy_Utilization_rpt.pdf (accessed Oct. 25, 2016).

DOI: 10.1021/jacs.6b11301
J. Am. Chem. Soc. 2017, 139, 2672−2681